14th IEA Heat Pump Conference
15-18 May 2023, Chicago, Illinois

Characterization of the fluid flow phenomena in an ejector for a high temperature heat pump

Manuel Schieder[a,*], Constantin Zenz[a,b], Julian Unterluggauer[a], Michael Lauermann[a], Adam Buruzs[a], Veronika Wilk[a], Thomas Fleckl[a], Christoph Reichl[a]

[a]AIT Austrian Institude of Technology GmbH, Giefinggasse 4, 1210 Vienna, Austria
[b]TU Wien Institute for Production Engineering E311, Karlsplatz 13, 1040 Vienna, Austria

Abstract

Decarbonization of industrial processes is one important step towards a sustainable future. The usage of high-temperature heat pumps to provide heat for industrial processes is a promising way towards that goal. Heat pumps used for such high temperature applications have a large difference between condenser and evaporator pressure and therefore the losses due to irreversible dissipation within the expansion process are high. To make high-temperature heat pumps more efficient and therefore interesting for industrial applications, the ejector, which is an alternative expansion device to replace the conventional throttle valve, is investigated. The flow inside an ejector of a high temperature heat pump is simulated numerically to gain better understanding of the underlying fluid flow phenomena, its applicability to heat pump cycles and to give an outlook on possible cycle efficiency improvements. To reduce the computational demand of simulating the two-phase flow inside the ejector and to avoid the need for experimental-based fine-tuning as opposed to a full multiphase model, the Homogeneous Equilibrium Model (HEM), which assumes thermal and mechanical equilibrium between both phases, is applied. This model was implemented into the commercial Computational Fluid Dynamics (CFD) software Ansys Fluent. The main flow features are analyzed, and phenomena occurring at unfavorable operating points, obtained through an unsuitable geometry, are identified.

Selection and/or peer-review under the responsibility of the organizers of the 14th IEA Heat Pump Conference 2023.

Keywords: High-temperature heat pump, CFD, Ejector

1. Introduction

Performance enhancement of high temperature heat pump systems is an important topic to facilitate a change in industrial energy systems. One way is to do cycle modification with the intentions of decreasing the electrical energy input under the restrictions of as low costs as possible. Therefore, the introduction of a two-phase ejector has become a promising cycle modification recently. Contrary to an ordinary expansion valve, the ejector recovers some of the expansion energy which is normally wasted in throttling processes. It reduces the compressor work by raising the suction pressure to a higher level, which directly leads to an improvement of the COP. Nakagawa et al. [1] experimentally analyzed ejectors and achieved a COP increase of up to 26%. Moreover, the ejector technology also leads to an evaporator size reduction as it provides a flash gas bypass. The technology itself is not new, as in 1990 Kornhauser [1] analyzed the thermodynamic performance of the ejector expansion refrigeration cycle using R12 as a working fluid.
To improve the design of ejectors CFD has become a valuable tool to enhance the performance. For a given ejector geometry, there exists only a small bandwidth of operating conditions that is leading to optimum efficiency [3][4][5].

Smolka et al. [6] developed a Homogeneous Equilibrium Model (HEM) to perform CFD simulations of a two-phase transcritical CO_2 ejector with a commercial CFD code without having to employ a full multiphase

* Corresponding author. Tel.: +43 50550-6602; fax: +43 50550-6679
E-mail address: manuel.schieder@ait.ac.at

model, as through the assumption of a homogeneous equilibrium, the governing equations can be used in their single-phase formulation. Bodys et al. [7] expanded the model of Smolka et al. [6] to account for thermodynamic metastability effects, which was realized through solving an additional equation for the vapor quality which includes a relaxation factor to be experimentally tuned. This addition to the homogeneous model led to an improvement of the prediction of CO_2 ejectors with subcritical inlet conditions. Yazdani et al. [8] used a mixture model to simulate the two-phase flow of CO_2 in an ejector. The mass transfer between the phases was modeled including both boiling and cavitation phenomena. Additionally, a slip velocity between the phases was included in the model. The analysis did not show a better accuracy in predicting key performance parameters of an ejector than simpler models like that of [7]. Biferi et al. [9] used the HEM of [6] to simulate a supersonic ejector with R134 as working fluid. The simplification of constant material properties except for those of density and speed of sound was made without drawbacks in accuracy.

Zhu et al. [10] showed that their 2D axisymmetric CFD simulation can predict the entrainment ratio with good accuracy (<10% error) compared to their measurements using R141b as working fluid.

In this work the HEM approach is used to model the flow phenomena inside the given R600 (butane) ejector. The extracted data from 2D-axisymmetric CFD simulations is analyzed and compared to experimental results. The results of this paper are partly based on the work of Zenz [11].

2. Heat pump cycle

The ejector in a heat pump cycle fulfils two purposes, first mixing of the high-pressure with the low-pressure flow and secondly pressure recovery by expansion. It consists of a primary inlet where the fluid is in a liquid state, a secondary inlet also called suction inlet where the fluid is in a gaseous state and one outlet with mixed conditions. As there are different types of ejectors it must be noticed that the presented design can be characterized as a two-phase supersonic constant pressure mixing ejector. A high-pressure fluid enters through the primary inlet and accelerates in the motive nozzle which entrains a low-pressure fluid through the secondary inlet. After a mixing process and static pressure recovery in a diffuser, the fluid leaves the ejector at a pressure that lies between the two inlet pressures. In the motive nozzle the fluid reaches supersonic speed while at the beginning of the diffuser the Mach number is close to 1 so that no further acceleration occurs, and pressure recovery is obtained.

The idea of an ejector in a heat pump cycle is to replace the expansion valve which has the purpose of converting the potential energy of the high-pressure fluid into kinetic energy as it is accelerated. Therefore, the pressure level at the compressor inlet is increased which leads to lesser electric energy needed and as a result to an increase of the COP. In Figure 1 the heat pump cycle, using an ejector, is depicted. Based on the ejector technology applied, the vapor entering the compressor from the separator at state 1 lies at a higher-pressure level than that of the evaporator. The low-pressure vapor leaving the evaporator (10) enters the ejector through the secondary inlet (5) and is entrained by the high-pressure stream coming from the condenser and entering the ejector through the motive nozzle (4). After pressure recovery inside the diffuser, the mixed two-phase refrigerant leaves the ejector at a higher-pressure level (7) and is separated into vapor (1) and liquid (8) phases.

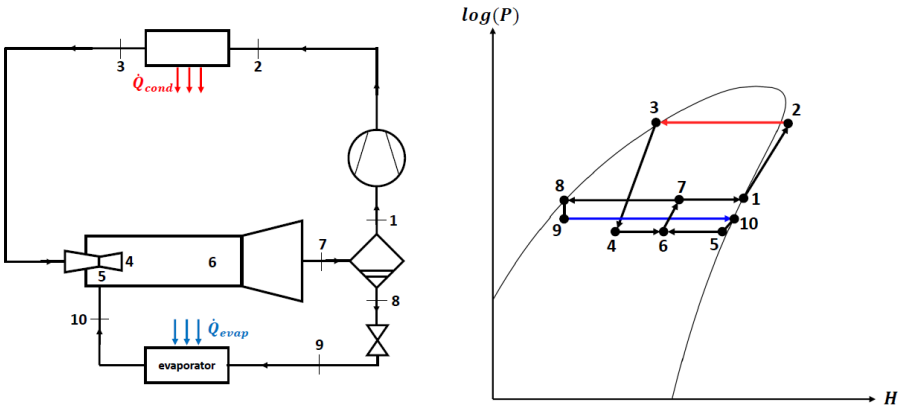

Fig. 1. Heat pump cycle and log(p)-H diagram. (see [11])

The ejector can be characterized by three key parameters. The first one is the entrainment ratio:

$$X = \frac{\dot{m}_{sec}}{\dot{m}_{prim}}, \tag{1}$$

with $\dot{m}_{sec}$ being the secondary inlet mass flow and $\dot{m}_{prim}$ the mass flow entering the motive nozzle at the primary inlet.
The second parameter is the suction pressure ratio:

$$\Pi_S = \frac{p_{out}}{p_{sec}}, \tag{2}$$

with p_{out} the absolute pressure at the outlet and p_{sec} the total pressure at the secondary inlet.
The last and third parameter is the ejector efficiency as it is defined by Elbel and Hrnjak [12]:

$$\eta_{ej} = X \frac{h(p_{out}, s_{sec}) - h(p_{sec}, s_{sec})}{h(p_{prim}, s_{prim}) - h(p_{out}, s_{prim})}, \tag{3}$$

Using the entrainment ratio X and enthalpy differences. In other words, the ejector efficiency can be described as the ratio of the amount of expansion work rate recovered to the maximum possible expansion work rate recovery potential of the ejector. Lawrence and Zhang et al. [13] found out that the ejector efficiency ranges from 20% to 30% for transcritical CO_2 heat pump cycles. They also mention that the best system performance may not occur when the ejector efficiency is at its peak for a given geometry.

3. Numerical Model

3.1. Geometry and Mesh

The geometry is designed by using an 1D simulation tool and is already published together with first measurement results by Schlemminger et al. [14].

Motive nozzle (A)	$D_{MN,1}$ [mm]	20
	$D_{MN,2}$ [mm]	4,4
	$D_{MN,3}$ [mm]	6,9
	$D_{MN,4}$ [mm]	26
	$\gamma_{MN,1}$ [°]	30
	$\gamma_{MN,2}$ [°]	10
	$\gamma_{MN,3}$ [°]	37
Mixing chamber (C)	L_{MCH} [mm]	11
	D_{TIP} [mm]	8,53
Suction nozzle (B) And Diffusor (D)	D_{SN} [mm]	38
	γ_{SN} [°]	37
	D_{MIX} [mm]	14
	L_{MIX} [mm]	112
	D_{DIF} [mm]	36
	γ_{DIF} [°]	5

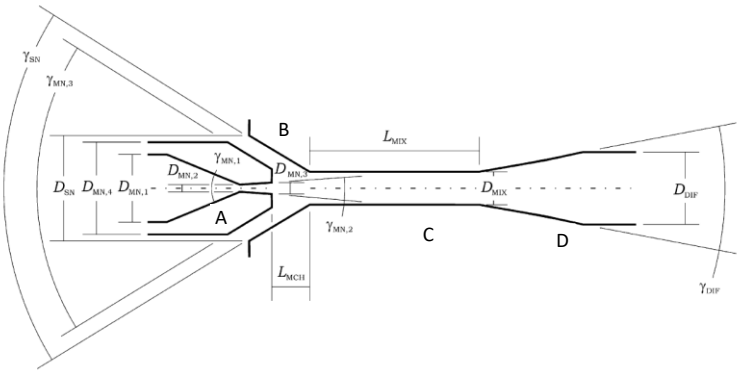

Fig. 2. Ejector design according to [14].

The domain is meshed using Ansys 19 Workbench to generate a full hexahedral grid with 167000 cells which is depicted in Figure 3.

The maximum skewness is well below 0.5 and refinements at the walls are included to keep the y^+ at a reasonable value (area-weighted average ≈ 2.5). The cells are stretched in axial direction which is increasing their aspect ratio in regions such as the mixing chamber and the diffuser, as there exists a clear direction of convective transport and therefore, the number of needed cells can be significantly reduced. Inside the primary nozzle and where the primary and secondary exit meet, the aspect ratio is kept near unity.

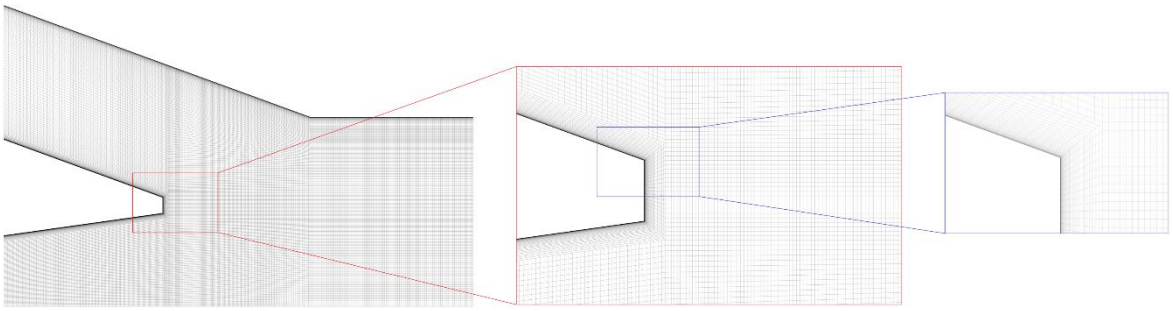

Fig. 3. Computational grid (167 000 cells).

3.2. Numerical setup and Boundary conditions

The boundary conditions are chosen accordingly to Schlemminger et al. [14] and are summarized in Table 1. The refrigerant entering the ejector through the motive nozzle is subcooled. However, in [14] it was assumed that a vapor quality of 2.7% was present at the primary inlet. Therefore, a two-phase state corresponding to a vapor quality of 2.7% was used as boundary condition for the value of enthalpy at the primary inlet. With the energy equation being enthalpy-based the temperature is not a variable used by the solver. The whole case is set up as a 2D-domain using Ansys 19 Fluent for steady-state simulations. To setup the Homogeneous Equilibrium Model, the energy equation needs to be solved in the enthalpy-based form. This is done with a User Defined Scalar (UDS), solving an additional transport equation for the enthalpy. Moreover, the material properties are updated by calling an User Defined Function (UDF) that contains the C-code to perform a bilinear interpolation in order to obtain material properties as functions of pressure and enthalpy based on the REFPROP 10.0 database [15]. To model turbulence the k-ω-SST taking compressibility effects into account is used. All equations are solved using first-order upwind schemes, except for pressure, where a second order pressure interpolation scheme is chosen. Second-order schemes are known to be more accurate and less diffusive, but also more numerical unstable. The drawback in accuracy of a first-order scheme over a second order scheme (given they are both of the same type, e.g. upwind schemes) can be compensated by using a denser computational grid. For the two-dimensional simulations performed in this work it was noticed that an increase in cell density comes at less computational cost than the needed measures to bring a simulation using second-order upwind schemes to convergence.

Table 1 Boundary conditions for R600 ejector

Boundary Condition	Value
Primary inlet total pressure (bar)	21.39
Primary inlet vapor quality (%)	2.7
Secondary inlet total pressure (bar)	4.3
Secondary inlet superheating ΔT (K)	8.06
Outlet static pressure (bar)	5.845

3.3. Homogeneous Equilibrium Model

To lower the computational demand, the Homogeneous Equilibrium Model was used as a two-phase model. In this model the liquid and the vapor phase are assumed to be in a thermal and mechanical equilibrium, meaning that pressure, temperature, velocity, turbulence kinetic energy and turbulence dissipation rate are the same in both phases [6].

All properties are a function of the specific enthalpy and the pressure. Since Ansys Fluent uses the temperature as an independent variable for the energy equation, an enthalpy-based energy equation was implemented, using the specific enthalpy as an independent variable. This was implemented as an UDS in the program.

The general form of a steady state transport equation of an arbitrary scalar ϕ (with Favre averaged quantities denoted with tilde and Reynolds averaged quantities denoted with a macron) in ANSYS Fluent has the form [6][16]:

$$\boldsymbol{\nabla} \cdot \left(\rho \tilde{\boldsymbol{u}} \tilde{\phi}\right) = \boldsymbol{\nabla} \cdot \left(\Gamma \boldsymbol{\nabla} \tilde{\phi}\right) + \dot{S}_{\phi}, \tag{4}$$

with $\dot{S}_{\phi}$ being an additional source term and Γ the diffusion coefficient of the scalar ϕ. The enthalpy-based energy equation for the implementation in Ansys Fluent has the following form, according to [6]:

$$\boldsymbol{\nabla} \cdot \left(\rho \tilde{\boldsymbol{u}} \tilde{h}\right) = \boldsymbol{\nabla} \cdot \left(\Gamma_h \boldsymbol{\nabla} \tilde{h}\right) + \dot{S}_{h1} + \dot{S}_{h2} + \dot{S}_{h3}, \tag{5}$$

with Γ_h being the diffusivity of h:

$$\Gamma_h = \frac{\lambda}{c_p} + \frac{\mu_t}{\sigma_t}. \tag{6}$$

where λ denotes the thermal conductivity, c_p the specific heat capacity at constant pressure, μ_t the turbulent viscosity and σ_t the turbulent Prandtl number.

The source terms represent the mechanical energy $\dot{S}_{h1}$, the irreversible dissipation of kinetic energy variations $\dot{S}_{h2}$ and the dissipation of turbulent kinetic energy $\dot{S}_{h3}$. These source terms have the following form [6]:

$$\dot{S}_{h1} = \tilde{\boldsymbol{u}} \cdot \boldsymbol{\nabla} \bar{p}, \tag{7a}$$

$$\dot{S}_{h2} = (\mu + \mu_t)\left\{2\left[\left(\frac{\partial \tilde{u}}{\partial x}\right)^2 + \left(\frac{\partial \tilde{v}}{\partial y}\right)^2 + \left(\frac{\partial \tilde{w}}{\partial z}\right)^2\right] + \left(\frac{\partial \tilde{u}}{\partial y} + \frac{\partial \tilde{v}}{\partial x}\right)^2 + \left(\frac{\partial \tilde{u}}{\partial z} + \frac{\partial \tilde{w}}{\partial x}\right)^2 + \left(\frac{\partial \tilde{v}}{\partial z} + \frac{\partial \tilde{w}}{\partial y}\right)^2 - \frac{2}{3}(\boldsymbol{\nabla} \cdot \tilde{\boldsymbol{u}})^2\right\} - \frac{2}{3}\bar{\rho} K \boldsymbol{\nabla} \cdot \tilde{\boldsymbol{u}}, \tag{7b}$$

$$\dot{S}_{h3} = -\bar{\rho} \tilde{\boldsymbol{u}} \cdot \boldsymbol{\nabla} K. \tag{7c}$$

For the implementation into Ansys Fluent, using the axisymmetric solver, all source terms need to be implemented in cylindrical coordinates, leading to:

$$\dot{S}_{h1} = \tilde{u}_r \frac{\partial \bar{p}}{\partial r} + \tilde{u}_\theta \frac{1}{r}\frac{\partial \bar{p}}{\partial \theta} + \tilde{u}_z \frac{\partial \bar{p}}{\partial z}, \tag{8a}$$

$$\dot{S}_{h2} = (\mu + \mu_t)\left\{2\left[\left(\frac{\partial \tilde{u}_r}{\partial r}\right)^2 + \left(\frac{1}{r}\frac{\partial \tilde{u}_\theta}{\partial \theta} + \frac{\tilde{u}_r}{r}\right)^2 + \left(\frac{\partial \tilde{u}_z}{\partial z}\right)^2\right] + \left[\frac{\partial}{\partial r}\left(\frac{\tilde{u}_\theta}{r}\right) + \frac{1}{r}\frac{\partial \tilde{u}_r}{\partial \theta}\right]^2 + \left(\frac{1}{r}\frac{\partial \tilde{u}_z}{\partial \theta} + \frac{\partial \tilde{u}_\theta}{\partial z}\right)^2 + \left(\frac{\partial \tilde{u}_r}{\partial z} + \frac{\partial \tilde{u}_z}{\partial r}\right)^2 - \frac{2}{3}(\boldsymbol{\nabla} \cdot \tilde{\boldsymbol{u}})^2\right\} - \frac{2}{3}\bar{\rho} K \boldsymbol{\nabla} \cdot \tilde{\boldsymbol{u}}, \tag{8b}$$

$$\dot{S}_{h3} = -\bar{\rho}\left(\tilde{u}_r \frac{\partial K}{\partial r} + \tilde{u}_\theta \frac{1}{r}\frac{\partial K}{\partial \theta} + \tilde{u}_z \frac{\partial K}{\partial z}\right). \tag{8c}$$

Since the velocities and derivatives in an axisymmetric simulation are zero, the source terms reduce to the following form:

$$\dot{S}_{h1} = \tilde{u}_r \frac{\partial \bar{p}}{\partial r} + \tilde{u}_z \frac{\partial \bar{p}}{\partial z}, \tag{9a}$$

$$\dot{S}_{h2} = (\mu + \mu_t)\left\{2\left[\left(\frac{\partial \tilde{u}_r}{\partial r}\right)^2 + \left(\frac{\tilde{u}_r}{r}\right)^2 + \left(\frac{\partial \tilde{u}_z}{\partial z}\right)^2\right] + \left(\frac{\partial \tilde{u}_r}{\partial z} + \frac{\partial \tilde{u}_z}{\partial r}\right)^2 - \frac{2}{3}(\boldsymbol{\nabla} \cdot \tilde{\boldsymbol{u}})^2\right\} - \frac{2}{3}\bar{\rho} K \boldsymbol{\nabla} \cdot \tilde{\boldsymbol{u}}, \tag{9b}$$

$$\dot{S}_{h3} = -\bar{\rho}\left(\tilde{u}_r \frac{\partial K}{\partial r} + \tilde{u}_z \frac{\partial K}{\partial z}\right), \tag{9c}$$

with the divergence of the velocity, assuming that velocity and derivatives in angular direction are zero:

$$\boldsymbol{\nabla} \cdot \tilde{\boldsymbol{u}} = \frac{\partial \tilde{u}_r}{\partial r} + \frac{\tilde{u}_r}{r} + \frac{\partial \tilde{u}_z}{\partial z}. \tag{10}$$

In the general form of cylindrical coordinates, the z-axis is considered as the symmetry axis. Ansys Fluent specifies the x-axis as the symmetry axis. Therefore, for the implementation in Ansys Fluent all terms in z-direction need to be implemented as x-direction terms.

4. Results

The mass flow rate and entrainment ratio were, in the experiment, measured as $\dot{m}_{\text{prim}} = 0.127$ kg/s and $X = 0.46$, respectively [13]. The simulation over-predicts the mass flow rate by 30% up to 45% and the entrainment ratio by 20% up to 50%, depending on the value of inlet vapor quality. The unsatisfactory prediction of mass flow rates by the HEM was also concluded by Bodys et al. [7] for subcritical inlet conditions (for CO_2 as working fluid). Therefore, they extended the underlying model to incorporate non-equilibrium effects. This led to an agreement between experimental and simulated mass flow rates of less than 10%. However, this model needs to be calibrated by a set of experiments which in not available for the presented R600 ejector.

The influence of vapor quality at the primary inlet on the primary mass flow rate and the entrainment ratio is shown in Figure 4. With an increase of the vapor quality the density decreases and therefore the mass flow changes quickly. However, the entrainment ratio X increases which suggests that the effect of the lower primary inlet mass flow is dominant over the effect on the physical process of entrainment.

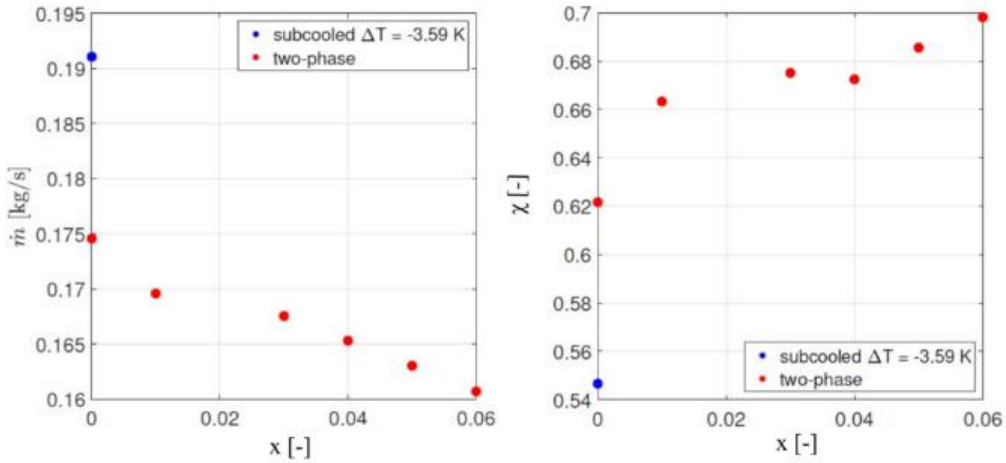

Fig. 4. Primary inlet mass flow rate $\dot{m}$ (left) and entrainment ratio $\boldsymbol{X}$ (right) for subcooled primary inlet condition and different levels of primary inlet vapor quality. (see [11])

Figure 5 shows the variation of static pressure along the ejector axis and wall compared to six measurement points obtained by the experiments published in [14]. In the mixing zone a deviation of the calculated pressure from experimental measurements is noticeable. This is also the location in which oblique shock waves occur. This might have affected the measurement results. However, specific potential errors in measurements due to condensation at the drilled hole for the pressure measurement, as well as thermal effects cannot be quantified.

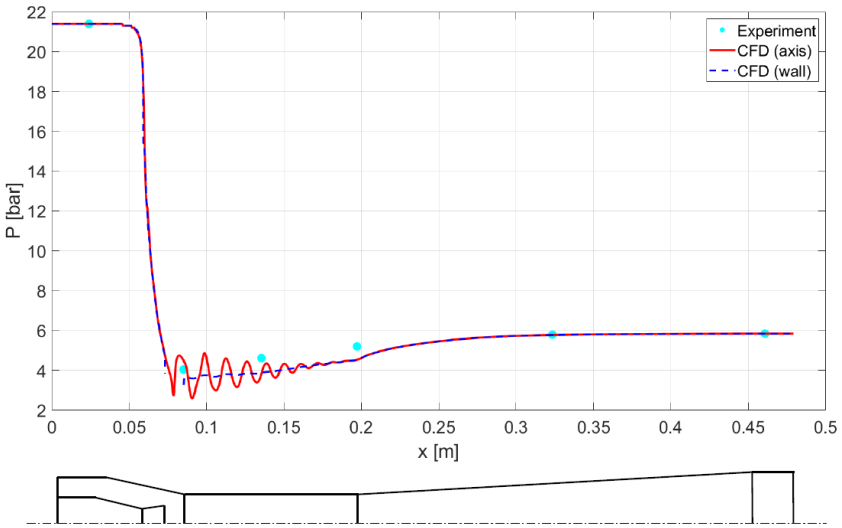

Fig. 5. Static pressure along the ejector axis and the wall, as well as experimental pressure measurements from [14]. (see [11])

Figure 6 shows the Mach number along the axis of the ejector. The oscillations in the mixing chamber correspond to supersonic shocks which can be noticed in the contour plot showed in Figure 7.

The velocity is decreasing, and no shocks are appearing at the beginning of the diffuser, which is a must have condition to guarantee the desired pressure recovery. This behavior can also be seen in the contour plot of the Mach number in Figure 7.

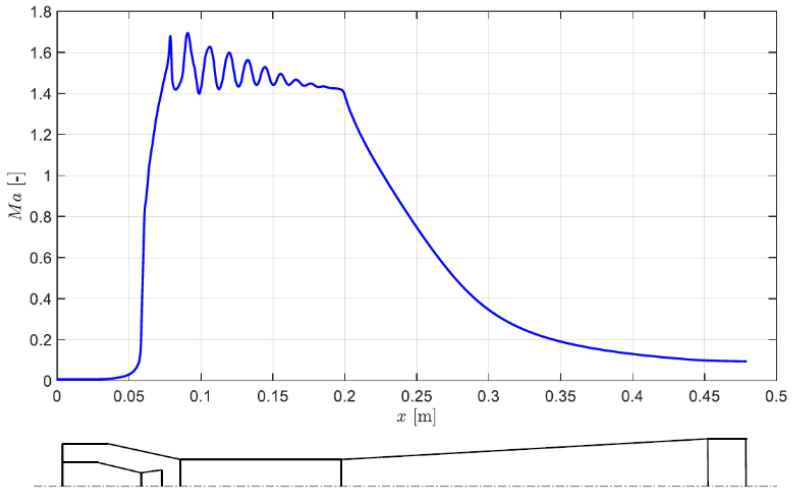

Fig. 6. Mach number along the ejector axis. (see [11])

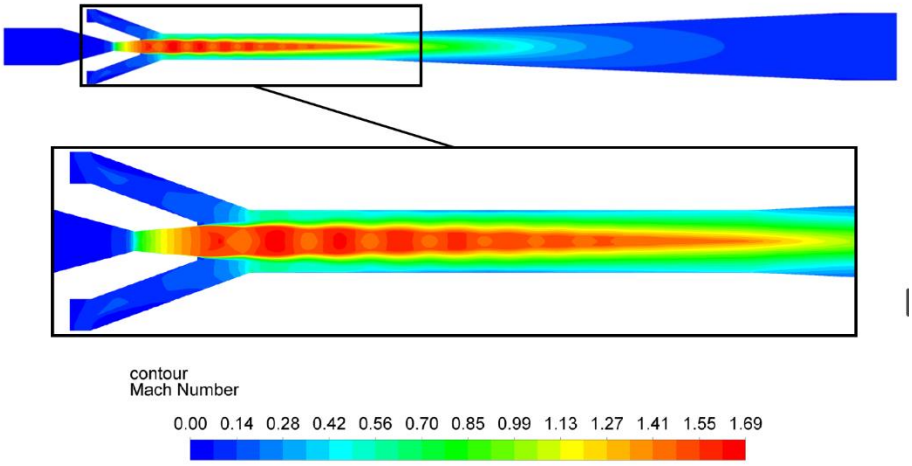

Fig. 7. Contour plot of the Mach number. (see [11])

How sensible the ejector design reacts to minor geometry variation in the motive nozzle can be seen in Figure 8. The primary nozzle throat and exit diameter are increased while keeping the converging and diverging angle constant, and the secondary nozzle cross-sectional area is decreased. In contrast to Figure 7 higher Mach numbers are reached and the flow stays supersonic until reaching the beginning of the diffuser, where a crucial shock occurs. As a result, boundary layer separation occurs and a recirculation region at the beginning of the diffuser forms. This leads to a performance drop with a decrease of the entrainment ratio to $X = 0.082$. Although, the simulation model is not able to capture non-equilibrium effects, qualitative conclusions on the suitability of an ejector geometry can be drawn. This model is especially interesting for drawing relative comparisons between different ejector geometries.

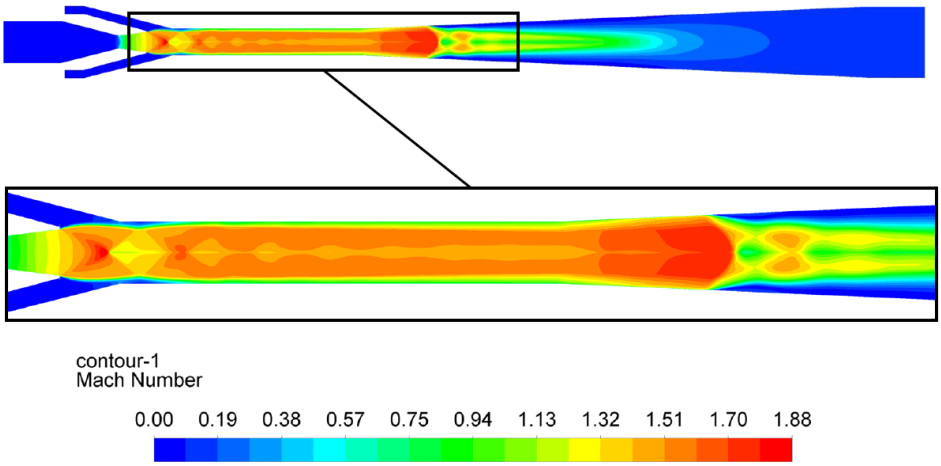

Fig. 8. Contour plot of the Mach number for a geometry variation of the motive nozzle. (see [11])

5. Conclusion

For the evaluation of the ejector performance in a high-temperature heat pump a CFD analysis was conducted.

A homogeneous equilibrium model was implemented in Ansys Fluent to allow for computationally affordable calculations of the two-phase flow. The benefit of the model is, that it does not need experimental fine-tuning, which is difficult, given that currently heat pumps featuring an ejector are still a topic of research and not commercially available. Even though the mathematical model is not capable of capturing metastability

effects, and therefore mass flow rate predictions are sometimes unsatisfactory, the model can still be used to make interesting qualitative observations. Furthermore, geometry shape optimizations can be extracted. Besides the limitations of the HEM approach, comparisons between different ejector geometries can be drawn. Concerning future work, a broader range of experimental data for ejectors operated under heat pump conditions is needed to calibrate more reliable numerical models. This is of importance as the main quantities of interest for heat pump cycle simulations, the mass flow rates and entrainment ratio, are found to be strongly affected by non-equilibrium thermodynamics. For further work, a subcooled state in the motive nozzle flow should be achieved in the experiments since the given ejector was originally designed for those conditions.

6. Copyright

By submittal of his or her full paper to the International Energy Agency for the 14th Heat Pump Conference, the author(s) assumes full responsibility for ensuring that his or her paper does not infringe on another party's intellectual property rights, which include copyright and agree that the paper has not previously been submitted for publication elsewhere. Furthermore, the author, by submittal of his or her conference paper to the conference, grants publishing rights of that paper to the Agency for the 14th Heat Pump Conference, which may:

1. Publish or arrange to publish the paper as part of the Conference proceedings,
2. Copy and distribute the paper in its entirety in print and electronic form, and
3. Copy and distribute excerpts from the paper.

Acknowledgements

This publication was conducted within the projects "ETHP" (FFG project number: 40165847) and "VWE" (FFG project number: 871723).
This project is funded by the Austrian national Research Funding Agency (FFG).

Nomenclature

Abbreviations

CFD	Computational Fluid Dynamics
COP	Coefficient of Performance
UDF	User Defined Function
UDS	User Defined Scalar

Greek Symbols

η_{ej}	Ejector efficiency
Γ	Diffusion coefficient
λ	Thermal conductivity
μ	Dynamic viscosity
μ_t	Turbulent viscosity
ϕ	Spare variable
Π_s	Suction pressure ratio
ρ	Density
σ_t	Turbulent Prandtl number

Latin Symbols

c_p	Specific heat capacity at constant pressure

h	Specific enthalpy
K	Turbulence kinetic energy
$\dot{m}$	Mass flow rate
p	Pressure
r	Radius
r, θ, z	Direction vector components in cylindrical coordinates
s	Specific entropy
$\dot{S}$	Source term in transport equation
$\boldsymbol{u}$	Velocity vector
u, v, w	Velocity components in cartesian coordinates
u_r, u_θ, u_z	Velocity components in cylindrical coordinates
x, y, z	Direction vector components in cartesian coordinates
X	Entrainment ratio

References

[1] Nakagawa, M., Marasigan, A., Matsukawa, T., and Kurashina, A. (2011). Experimental investigation on the effect of mixing length on the performance of two-phase ejector for CO2 refrigeration cycle with and without heat exchanger. International Journal of Refrigeration, 34(7):1604–1613. http://dx.doi.org/10.1016/j.ijrefrig.2010.07.021.

[2] Kornhauser AA. (1990). The use of an ejector as a refrigerant expander. Proceedings of USNC/IIR-Purdue refrigeration conference, USA.

[3] Grazzini G., Milazzo A., and Mazzelli F..(2018) Ejectors for Efficient Refrigeration. Design, Applications and Computational Fluid Dynamics. Springer. https://doi.org/10.1007/978-3-319-75244-0

[4] Varga S., Oliveira A. C., and Diaconu B.. (2009). Influence of geometrical factors on steam ejector performance - A numerical assessment. International Journal of Refrigeration 32, pp. 1694-1701. https://doi.org/10.1016/j.ijrefrig.2009.05.009

[5] Banasiak K. and Hafner a.. (2011). 1D Computational model of a two-phase R744 ejector for expansion work recovery. International Journal of Thermal Sciences 50, pp. 2235-2247. https://doi.org/10.1016/j.ijthermalsci.2011.06.007

[6] Smolka, J., Bulinski, Z., Fic, Z., Nowak, A. J., Banasiak, K., and Hafner, A. (2013). A computational model of a transcritical R744 ejector based on a homogeneous real fluid approach. Applied Mathematical Modelling, 37(3):1208–1224. http://dx.doi.org/10.1016/j.apm.2012.03.044.

[7] Bodys J. et al. (2020). Non-equilibrium approach for the simulation of CO2 expansion in two-phase ejector driven by subcritical motive pressure. International Journal of Refrigeration 114, pp. 32-46. http://dx.doi.org/10.1016/j.ijrefrig.2020.02.015.

[8] Yazdani M., Alahyari A.A., and Radcli T. D.. (2012). Numerical modeling of two-phase supersonic ejectors for work-recovery applications. In: International Journal of Heat and Mass Transfer 55, pp. 5744-5753. https://doi.org/10.1016/j.ijheatmasstransfer.2012.05.071

[9] Biferi G. et al. (2016). CFD modelling of the condensation inside a supersonic ejector working with R134a. Energy Procedia 101, pp. 1232-1239. https://doi.org/10.1016/j.egypro.2016.11.138

[10] Zhu Y., Cai W., Wen C., Li Y.. (2009). Numerical investigation of geometry parameters for design of high performance ejectors,Appl. Therm. Eng., 29 ,pp. 898-905. https://doi.org/10.1016/j.applthermaleng.2008.04.025

[11] Zenz, C. (2020). Numerical Analysis of Fluid Flow and Heat Transfer Characteristics of Ejectors and Vortex Tubes [Master's Thesis, TU Wien]. https://doi.org/10.34726/hss.2020.64243

[12] Elbel, S. and Hrnjak, P. (2008). Experimental validation of a prototype ejector designed to reduce throttling losses encountered in transcritical R744 system operation. International Journal of Refrigeration, 31(3):411–422. http://dx.doi.org/10.1016/j.ijrefrig.2007.07.013

[13] Zhang, Z., Feng, X., Tian, D., Yang, J., & Chang, L. (2020). Progress in ejector-expansion vapor compression refrigeration and heat pump systems. Energy Conversion and Management, 207, 112529. https://doi.org/10.1016/j.enconman.2020.112529

[14] Schlemminger, C., Kopp, C., Banasiak, K., Drexler-Schmid, G., Lauermann, M., Windholz, B., Zauner, C., & Baumhakel, A. (2019). Hochtemperatur Wärmepumpe mit Ejektor. *Deutsche Kälte- und Klimatagung 2019, Ulm.* DKV - Deutscher Kälte- und Klimatechnischer Verein.

[15] Lemmon, E. W., Bell, I. H., Huber, M. L., and McLinden, M. O. (2018). NIST Standard Reference Database 23: Reference Fluid Thermodynamic and Transport Properties-REFPROP, Version 10.0, National Institute of Standards and Technology

[16] ANSYS, Inc. (2022). Ansys® Fluent Theory Guide, Release 2022 R1. Canonsburg, USA, 2022.